

Journal of Seismic Exploration

ARTICLE

Quantifying the effects of micro-cracks on velocity anisotropy in lacustrine shales with variable sedimentary structures

Wenhui Tan^{1,2}, Weihua Liu^{1,2}, Yang Wang^{1,2}, and Hui Shen^{1,2}

¹SINOPEC Geophysical Research Institute Co., Ltd., Nanjing, Jiangsu, China ²SINOPEC Key Laboratory of Geophysics, Nanjing, Jiangsu, China

(This article belongs to the Special Issue: Seismic Wave Propagation Theories and Reservoir Characterization Technologies for Complex Anisotropic Media)

Abstract

Understanding the relationship between micro-cracks and elastic anisotropy is crucial for characterizing subsurface flow pathways, optimizing hydraulic fracturing, and enhancing seismic interpretation in unconventional shale reservoirs. Although clay content and total organic carbon (TOC) are recognized primary controls on anisotropy, the specific influence of sedimentary structures on micro-crack parameters (such as crack porosity, crack density, and aspect ratio) and their contribution to anisotropic behavior have not been fully quantified, particularly in lacustrine shales with varied sedimentary architectures. In this study, 17 shale samples were categorized into three sedimentary structural types: laminated, bedded, and massive, based on their microstructure characteristics. Ultrasonic velocity measurements were performed on 17 paired shale plugs under confining pressures to quantify the relationship between micro-crack parameters and elastic anisotropy. Experimental results reveal a clear difference in stress sensitivity of bedding-normal velocities: Laminated shales > bedded shales > massive shales, which are attributed to varying degrees of micro-crack alignment and density. Laminated shales exhibit the strongest anisotropic properties, followed by bedded shales, while massive shales show weak anisotropy. Velocity predictions from the Mori-Tanaka effective medium model are in good agreement with the measurements, validating its applicability for shales with diverse structures. Micro-crack analysis indicates a positive correlation between crack density/porosity and anisotropy magnitude. Notably, laminated shales are characterized by the highest crack porosity (0.012-0.015%), high clay content (average 40%), and moderate TOC, indicating a combined effect of composition and microstructure on anisotropy. This study highlights that sedimentary structure plays a key role in controlling micro-crack development and related anisotropy in lacustrine shales, with laminated shales exhibiting the most significant combined effect, thus improving the accuracy of minimum-horizontal-stress prediction and hydraulic-fracture design.

Keywords: Lacustrine shale; Micro-cracks; Thomsen anisotropic parameters; Ultrasonic experiment; Mori-Tanaka model

*Corresponding author: Yang Wang (wangyang.swty@sinopec.com)

Citation: Tan W, Liu W, Wang Y, Shen H. Quantifying the effects of micro-cracks on velocity anisotropy in lacustrine shales with variable sedimentary structures. *J Seismic Explor*. 2025;34(4):28-41. doi: 10.36922/JSE025340060

Received: August 18, 2025
Revised: September 12, 2025
Accepted: September 17, 2025
Published online: October 23.

2025

Copyright: © 2025 Author(s). This is an Open-Access article distributed under the terms of the Creative Commons Attribution License, permitting distribution, and reproduction in any medium, provided the original work is properly cited.

Publisher's Note: AccScience Publishing remains neutral with regard to jurisdictional claims in published maps and institutional affiliations.

1. Introduction

In recent years, lacustrine shale oil and gas reservoirs in China have emerged as a critical focus in the development of unconventional hydrocarbon resources. Shale is a selfgenerating and self-storing reservoir. Its unique properties make it a strategic target for boosting China's oil and gas reserves. 1-3 In the exploration and development of shale oil and gas, elastic anisotropy is the key geological attribute to determine the physical properties of reservoirs. Studies have shown that shale reservoirs generally exhibit significant anisotropic characteristics.^{4,5} This anisotropy controls wave propagation, fluid flow, and mechanical response. Consequently, it affects seismic imaging, log interpretation, reservoir characterization, and fracturing design. This characteristic has a direct impact on seismic imaging accuracy, logging interpretation reliability, reservoir physical characterization, and hydraulic fracturing scheme design by controlling seismic wave propagation law, seepage capacity, and mechanical response.⁶⁻⁹ Accurately characterizing the anisotropic characteristics of shale can not only improve the prediction accuracy of seismic data on reservoir boundary and quality, but also effectively reduce engineering risks and costs by optimizing exploration and development strategies. However, due to the influence of geological deposition and diagenesis, the coupling of horizontal bedding, organic-inorganic mineral facies, and pore space in organic-rich shale leads to the extremely complex formation mechanism of elastic anisotropy, which brings severe challenges to the establishment of a universal anisotropy model. At the micro-scale, micro-cracks are the key factor controlling the anisotropy of shale, and there is still a significant uncertainties remain in quantifying the influence mechanism of micro-cracks on velocity anisotropy. In addition, the differences in experimental conditions (such as stress state and fluid properties) and the diversity of theoretical models (such as equivalent medium theory and discrete fracture network simulation) in the current research lead to the lack of comparability between different results, and a unified scientific understanding has not yet been established. 10-12

As a typical fine-grained sedimentary rock, shale exhibits significant anisotropy shaped by micro-cracks, the preferred orientations of platy clay particles, and lenticular kerogen. Researchers worldwide have conducted extensive experimental studies on shale samples to identify the controlling factors of intrinsic anisotropy. Vernik and Liu¹³ performed ultrasonic measurements on the Bakken shale (USA). They observed maximum elastic anisotropy at total organic carbon (TOC) values of 15–20%. This reveals the critical role of organic matter content in shale elasticity; bedding-parallel organic matter may significantly

influence medium anisotropy by altering mineral grain contacts or micro-crack alignment. Notably, there are obvious geological differences in the influence of organic matter on anisotropy. The anisotropy of Wufeng-Longmaxi Formation shale in China has no obvious correlation with organic matter content, while the organic matter content of Bakken shale in the United States and Bazhenov shale in Russia is the key controlling factor of anisotropy. This difference is attributed to the different maturity, occurrence form, and distribution characteristics of organic matter. Laminated clay minerals represent another key factor. Comparative studies by Sone and Zoback¹⁴ on North American shales (Barnett, Haynesville, Eagle Ford) showed a significant positive correlation between clay content and anisotropy intensity, consistent with theories with transversely isotropic proposed by Hornby et al.15 and Sayers¹⁶ that laminated clay induces the formation of transversely isotropic shale. Further studies indicate that preferred orientation of clay platelets directly affects shale elastic parameters. 17-24 Liu et al. 12 measured ultrasonic pulses in Longmaxi Shale and found a 0.82 correlation between clay content and velocity anisotropy parameters: The higher the degree of clay orientation, the more significant the anisotropy characteristics. Liu et al.25 studied Jurassic lacustrine shale from the Sichuan Basin and proposed an "effective parameter" (total porosity + clay content + kerogen volume) to distinguish elastic and anisotropic characteristics among four lithofacies, based on ultrasonic velocity measurements under varying confining pressures.

In recent years, beyond studies on the intrinsic anisotropy of shale under high-pressure conditions, the fracture response information embedded in velocity variations with confining pressure has become a research focus for scholars. Vernik²⁶ first quantified the dynamic relationship between micro-crack-induced anisotropy and mineral-oriented intrinsic anisotropy through confining pressure-velocity experiments on mature source rock shales: as confining pressure increases, progressive micro-crack closure leads to a decrease of anisotropy, while intrinsic anisotropy from preferred orientation clay/kerogen tends to stabilize. This achievement provides key mechanical insights into the anisotropy evolution of stress-sensitive reservoirs. Ciz and Shapiro²⁷ established a porositydeformation approach for transversely isotropic shales and, combined with ultrasonic measurement data from North Sea shale samples, inverted crack contribution through the confining pressure response of elastic moduli, verifying the dominant role of micro-crack closure in anisotropy. 11,28-31 These previous studies revealed the coupled relationship between cracks, confining pressure, and anisotropy through experimental observations, theoretical modeling, and numerical simulations. Nevertheless, the current rock

physics approach to inverting the response mechanism of cracks and reservoir parameters still faces multiple challenges. At present, the research on anisotropy induced by stress-induced cracks mainly focuses on marine shale. However, due to the complexity of the microstructure of la cuisine shale, the effective medium model is limited in its application. In addition, there are significant differences in the anisotropy values generated by stress-induced cracks in different lithofacies, underscoring the urgent need for more in-depth investigations in this domain.

In this study, we focus on lacustrine shales from the Songliao Basin in Northeast China. Based on their microstructural characteristics, these shales are classified into three lithofacies types. Using ultrasonic velocity measurement experiments and inversion based on the Mori-Tanaka (M-T) effective medium theory, we systematically investigate the anisotropic responses of stress-induced micro-cracks in lacustrine shales and elucidate the underlying mechanism by which micro-cracks contribute to shale anisotropy. The results offer critical experimental evidence and theoretical basis for predicting micro-crack development in lacustrine shale reservoirs via seismic data, as well as optimizing reservoir evaluation and development strategies.

2. Experimental methodology

2.1. Basic characteristics of the sample

Seventeen full-diameter shale samples used in this study were collected from a Cretaceous lacustrine reservoir located in Northeastern China. The mud shale in such a formation is frequently characterized by its large thickness, high TOC, moderate thermal maturity, and overpressure. 32-34 A total of 17 cylindrical plugs, each with a diameter of 25 mm and a length of approximately 50 mm, were drilled from the full-diameter samples along the bedding direction. The cylinders then underwent a drying process with a temperature of 80°C for over 48 h, until the sample weight does not vary. Subsequently, the porosity of each cylindrical shale sample is measured using the helium gas method.

TOC of each sample is measured by the Rock-Eval Pyrolysis tests. The results revealed that TOC of 17 samples ranges from 0.1 to 3.2%. The mineral composition of each shale sample was determined through the powder X-ray diffraction analysis (Figure 1). The collected shales are mainly composed of clay, quartz + feldspar + pyrite (QFP), and carbonate minerals. From the core photos and the thin section images in Table 1, the fine-grained rocks can be described as either laminated, bedded, or massive, 34,35 according to the thickness of beddings. The laminated rocks, with bedding thickness <10 mm, display obvious grain-size changes. The silt and clay laminae terminate

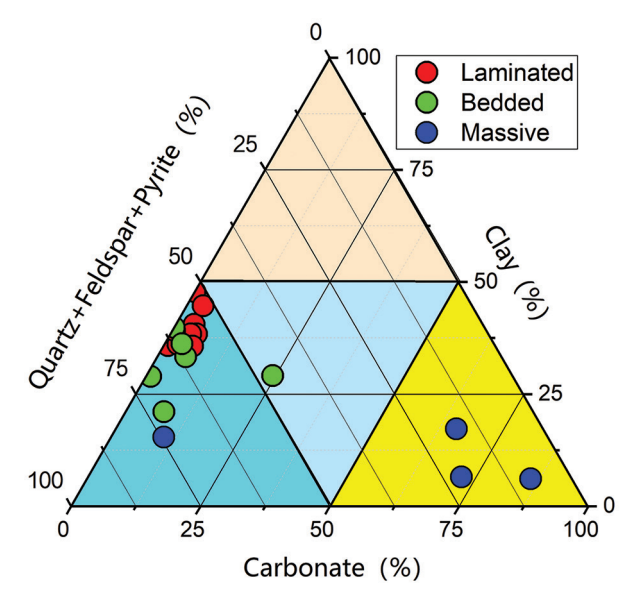


Figure 1. Ternary diagram for 17 shale samples with different sedimentary structures. The red circle represents laminated, the green circle represents bedded, and the blue circle represents massive.

sharply at their margins, as shown in Table 1. The bedding thickness of bedded rocks is normally >1 cm with silt or clay beddings alternately stacking together, as shown in Table 1. The massive samples, with bedding thickness larger than 50 cm, are distributed either near the 100%-carbonate-end or the 100%-QFP-end in the ternary diagram (Figure 1).

From Table 1, the development of micro-cracks varies with the sedimentary structures. In general, the microcracks are most developed in laminated shales, followed by bedded shales. Nearly no micro-cracks could be seen in the massive shales from the amplified thin section image. The development of micro-cracks in laminated shales could be attributed to two main reasons. From one aspect, in the weak plane between silt and clay laminae, it is easy to develop bedding cracks or diagenetic contraction cracks along bedding directions. From the other aspect, the stripped kerogen in laminated shales is at the peak of oil generation ($R_{\circ} \sim 1.3\%$). A mass of hydrocarbon would be generated and migrated along the weak plane between beddings, leaving hydrocarbon-expulsion micro-cracks behind.36 For bedded shales, the inter-bedded microcracks (at the silt-clay interfaces) dominate, while less hydrocarbon-expulsion micro-cracks develop. For massive shale, due to its homogeneous mineral composition and lack of laminae weak planes, only sporadically isolated contraction cracks develop.37,38

2.2. Measurement of anisotropic ultrasonic velocity

We performed ultrasonic velocity measurements on 17 horizontal shale samples by using the pulse

Table 1. Cores and thin sections of laminated shale, bedded shale, and massive shale

Samples	Cores	Thin sections	Descriptions
Laminated shale	AT REPORT OF THE PARTY.	Hydrocarbon-induced cracks A Bedding cracks	 Alternating deposition of silt and clay laminae, with thickness <10 mm. Bedding cracks, diagenetic contraction cracks, and hydrocarbon-expulsion cracks develop along bedding directions.
Bedded shale			 Bedding thickness is >1 cm with silt or clay beddings alternately stacking together. The inter-bedded micro-cracks (at the silt-clay interfaces) dominate.
Massive shale			 The mineral composition is uniform, lacking laminae or bedding interfaces. Micro-cracks are less developed.

transmission method.39 To gain velocities in different directions from one single horizontal plug, three pairs of P-wave transducers (0°, 45°, and 90° with respect to the symmetry axis) and two pairs of S-wave transducers (propagating along beddings, polarizing in both beddingnormal and bedding-parallel direction) were mounted in the sample, as shown in Figure 2. The central frequencies for P- and S-wave transducers were 1 MHz and 0.5 MHz, respectively. The horizontal shale was wrapped with the rubber sleeve and put into a confining vessel filled with silicon oil. The velocities were measured at varied confining pressures ranging from 5 MPa to 35 MPa. Five velocities were all measured in one single horizontal shale plug: $V_{p}(0^{\circ})$, $V_{p}(90^{\circ})$, $V_{p}(45^{\circ})$, $V_{sh}(90^{\circ})$, and $V_{sv}(90^{\circ})$, allowing for a thorough analysis of the full stiffness tensor and anisotropy of transversely isotropic (TI) shales. It is noteworthy that the relative systematic error in velocity measurements is approximately $\pm 1\%$ for P-waves and $\pm 2\%$ for S-waves.

Unconventional shales are often depicted to be a transversely isotropic medium with a vertical rotational symmetry axis (VTI). According to the anisotropic Hooke's law, a VTI medium can be characterized by five independent stiffnesses (C_{11} , C_{33} , C_{44} , C_{66} , C_{13}). With five direction-dependent velocities and the measured bulk density (ρ), five independent stiffnesses could be derived as follows:

$$C_{11} = \rho V_p^2 (90^\circ) \tag{I}$$

$$C_{33} = \rho V_p^2(0^\circ) \tag{II}$$

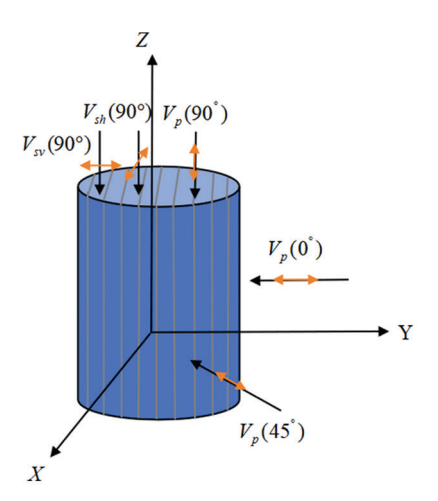


Figure 2. Schematic diagram of the direction-dependent velocity measurement with one-single-horizontal shale sample³⁹

$$C_{44} = \rho V_{cu}^2(90^\circ) \tag{III}$$

$$C_{12} = C_{11} - 2\rho V_{sh}^2 (90^\circ)$$
 (IV)

$$C_{13} = -C_{44} + \sqrt{\frac{(C_{11} + C_{44} - 2\rho V_p^2 (45^\circ))}{(C_{33} + C_{44} - 2\rho V_p^2 (45^\circ))}}$$
 (V)

Subsequently, P- and S-wave velocity anisotropy could be expressed with Thomsen's parameters, ε and γ , respectively⁴⁰:

$$\varepsilon = \frac{C_{11} - C_{33}}{2C_{33}} \tag{VI}$$

$$\gamma = \frac{C_{66} - C_{44}}{2C_{44}} \tag{VII}$$

3. Pressure-dependent properties

3.1. Experimental results

Figure 3 displays the directional velocities ($V_{\rm p}(0^{\rm o})$, $V_{\rm p}(90^{\rm o})$, $V_{\rm sh}(90^{\rm o})$, and $V_{\rm sv}(90^{\rm o})$) as a function of the applied confining pressure for three typical samples with laminated, bedded, and massive structure. Overall, despite the rock structure, all four velocities increase with the increasing pressure. Both P- and S-wave velocities in the bedding-normal direction ($V_{\rm p}(90^{\rm o})$ and $V_{\rm sv}(90^{\rm o})$) satisfy the following relationship: laminated < bedded < massive.

The pressure-dependent velocities in Figure 3, to some extent, reveal the effects of bedding-related micro-cracks.

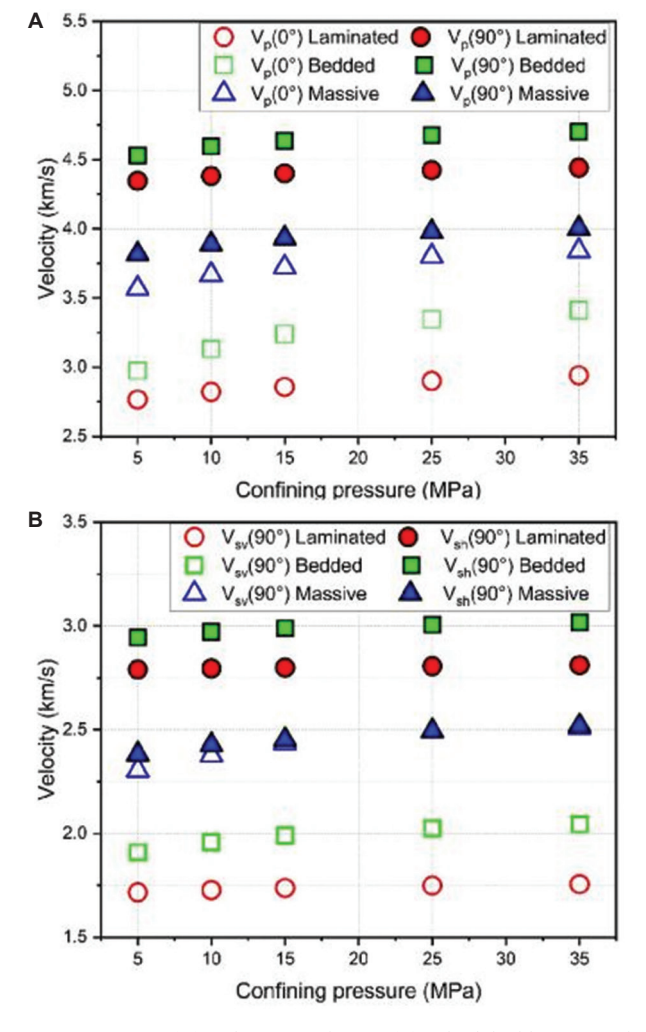


Figure 3. P-wave (A) and S-wave velocities (B) in both bedding-normal and bedding-parallel directions as a function of the applied confining pressure for three typical samples with laminated, bedded, and massive structure

In general, the bedding-normal velocities show strong non-linear behavior at low pressures and subsequently get flattened at high pressures, while the beddingparallel velocities are almost linear over the entire range of confining pressure.26 By assuming that the flattened bedding-normal velocities indicate all micro-cracks are closed at the highest pressure, 41 we define a stress sensitivity parameter, V/V(35MPa), to qualitatively characterize the effects of micro-cracks for three types of rocks. It should be noted that V denotes $V_{p}(0^{\circ})$ or $V_{sy}(90^{\circ})$ at the varied confining pressures (5 MPa, 10 MPa, 15 MPa, 25 MPa, and 35 MPa), while V(35MPa) suggests $V_p(0^\circ)$ or $V_{sy}(90^\circ)$ at the confining pressure of 35 MPa. Figure 4 shows the plot of the stress sensitivity parameter against the applied confining pressure for $V_{p}(0^{\circ})$ and $V_{sv}(90^{\circ})$. Both stress sensitivity parameters vary non-linearly up to 1 at the highest confining pressure, revealing a process of microcracks closure. The stress sensitivity of bedding-normal

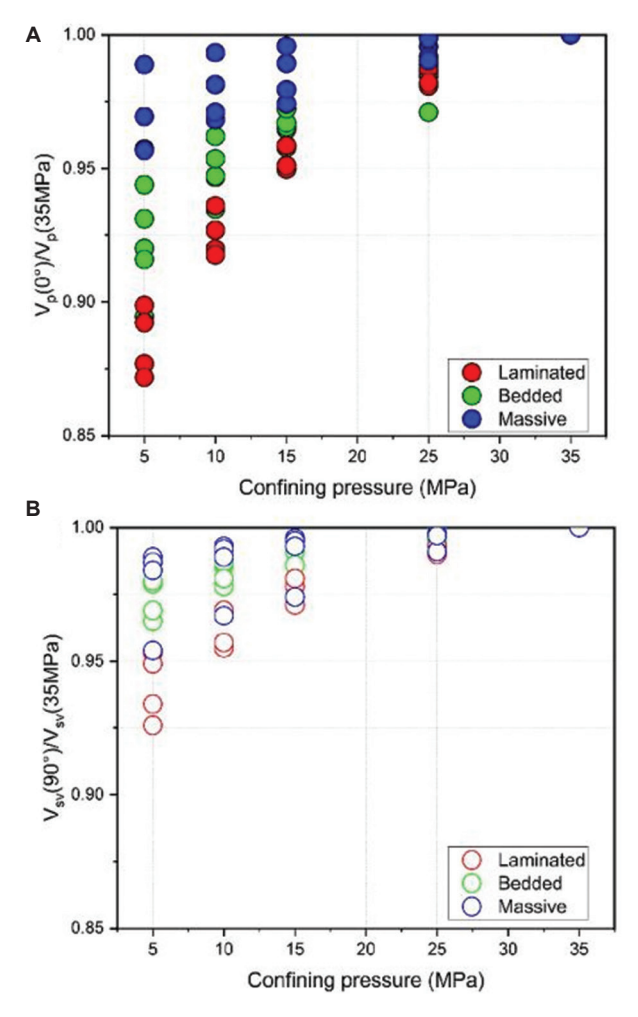


Figure 4. Stress sensitivity parameter as a function of the applied confining pressure for $V_{_0}(0^{\circ})$ (A) and $V_{_{\rm CV}}(90^{\circ})$ (B)

velocities relies on the rock structures, satisfying the following relationship: laminated > bedded > massive.

As shown in Figure 3, the bedding-parallel velocities are generally greater than the bedding-normal ones, especially for laminated and bedded shales, displaying obvious velocity anisotropy. The anisotropy degree of P- and S-wave velocities is expressed with ε and γ , calculated based on **Equations VI** and **VII**. Accordingly, Figure 5 shows plots of ε and γ against the applied confining pressure for three typical samples. Figure 5A shows both ε and γ for laminated and bedded samples decrease non-linearly as the confining pressure increases from 5 MPa to 25 MPa, and get relatively flattened at the subsequently confining pressure. However, ε and γ for the massive shale are much lower, combined with relatively constant values over the entire confining pressure range. Figure 5B presents a crossplot of Thomsen's

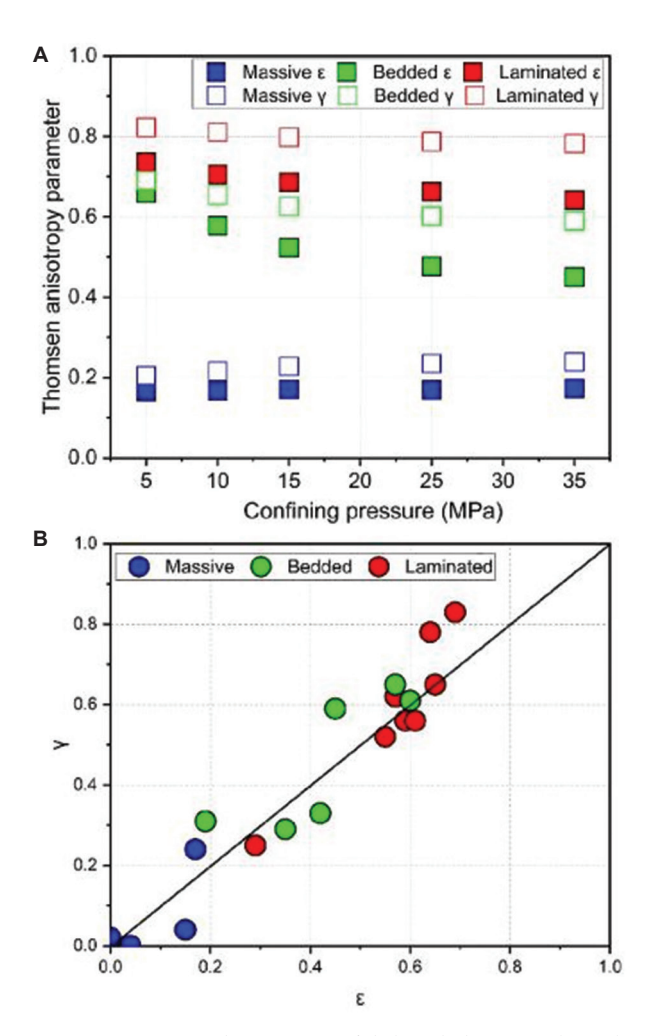


Figure 5. Anisotropic characteristics of shale with three typical samples. (A) ε and γ as a function of the applied confining pressure for three typical samples with laminated, bedded, and massive structure. (B) A plot of anisotropy parameter γ versus anisotropy parameter ε for three typical samples with laminated, bedded, and massive structure.

anisotropy parameters ε and γ for three structural types. Overall, ε and γ show a good positive linear correlation. The laminated samples exhibit stronger anisotropy, generally occupying higher values of both ε and γ =, while the massive samples cluster at lower values, and the bedded samples show an intermediate distribution.

3.2. Mechanism of shale anisotropy

Shale velocity anisotropy is frequently attributed to the combined effects of many intrinsic and extrinsic factors.8 Intrinsic velocity anisotropy primarily stems from three key mechanisms: The alternation of lithologies or laminae, the preferred orientation of clay platelets or kerogen, and the bedding-parallel micro-cracks. 13,42,43 Figure 5B shows a plot of γ versus ε at the highest confining pressure (35 MPa), revealing the effects of rock texture (laminated, bedded, massive) and mineral composition on intrinsic anisotropy. Based on Figure 5B, the anisotropy degree of 17 lacustrine shales satisfies the following relationship: laminated > bedded > massive. As shown in Figure 1, the total clay content ranges from 5% to 45%, with an average value of 40% for laminated shales and 32% for bedded shales. For Cretaceous shale reservoirs, clay minerals have thoroughly experienced the transition from smectite to illite. Clay minerals are dominated by illite and illitesmectite mixed layers with obvious preferred orientation along beddings after sedimentary compaction, resulting in relatively strong anisotropy. However, for massive shales, the anisotropy degree is relatively low due to the low clay content and lack of bedding texture. Besides, the kerogen tends to align subparallel to beddings with a striplike pattern for laminated and bedded shales, as shown in Table 1, further amplifying the velocity contrast in bedding-normal and bedding-parallel directions.

In addition, the pressure-dependent properties of bedding-normal velocities (Figure 4) and anisotropy parameters (Figure 5A) indicate that micro-cracks might be a non-negligible factor in evaluating shale anisotropy. As discussed in Table 1, micro-cracks mainly originate from two sources: Bedding-parallel micro-cracks and hydrocarbon-expulsion-induced micro-cracks. cracks are closed at in situ conditions. In the process of coring, these micro-cracks tend to open due to the stress relief. By applying confining pressure to the approximate in situ stress condition in the laboratory, these opened cracks close gradually, revealing the pressure-dependence of bedding-normal velocities. Conversely, the pressure dependence of velocities can, to some extent, be used to quantitatively evaluate the contribution of micro-cracks to shale anisotropy. In the next section, we will focus on the quantitative inversion and evaluation of micro-crack effects on anisotropy.

4. Effects of micro-cracks on shale anisotropy

4.1. M-T theory

To quantitatively evaluate the effects of micro-cracks on shale anisotropy, the key is to accurately invert micro-crack parameters from the pressure-dependent bedding-normal velocities (Figure 3). We employed the M-T theory,⁴⁴ which has been widely recognized for its capability to capture the intricate interactions between the micro-structural features of materials and their macroscopic mechanical properties.

Mori and Tanaka⁴⁴ established the relationship between the elastic modulus of rocks and their microscopic pore structure. The stiff moduli of rocks are expressed as:

$$K_{stiff} = \frac{K_0}{(1 + \phi_{stiff} / 1 - \phi_{stiff} P)}$$
(VIII)

$$G_{stiff} = \frac{G_0}{(1 + \frac{\phi_{stiff}}{1 - \phi_{stiff}}Q)}$$
(IX)

Where K_{stiff} and G_{stiff} are the effective bulk and shear modulus of rocks, when only stiff inter-particle pores exist. K_0 and G_0 are bulk and shear moduli of mineral grains, respectively. Φ_{stiff} indicates the porosity contributed from inter-particle pores. P and Q represent shape factors of stiff pores, which are related to the aspect ratio α of ellipsoidal pores and Poisson's ratio v_s of mineral grains, 41,45 as shown in **Equations X-XII**. By assuming that low-aspect-ratio micro-cracks (soft pores) are completely closed at extreme high confining pressure, K_{stiff} and G_{stiff} could be calculated through $V_p(0^\circ)$ and $V_{\text{sv}}(90^\circ)$ measured at confining pressure of 35 MPa, as shown in Figure 3. Based on **Equation VIII**, α can be obtained through the least squares regression of K_{criff} .

$$P = \frac{1 - \upsilon_{s}}{6(1 - 2\upsilon_{s})} \cdot \frac{4(1 + \upsilon_{s}) + 2\alpha^{2}(7 - 2\upsilon_{s}) - [3(1 + 4\upsilon_{s})]}{2\alpha^{2} + (1 - 4\alpha^{2})g + (\alpha^{2} - 1)(1 + \upsilon_{s})g^{2}}, \quad (X)$$

$$Q = \frac{4(\alpha^{2}-1)(1-\upsilon_{s})}{15\left\{8(\upsilon_{s}-1)+2\alpha^{2}(3-4\upsilon_{s})+[(7-8\upsilon_{s})-4\alpha^{2}(1-2\upsilon_{s})]g\right\}}$$

$$\cdot \begin{cases} 8(1-\upsilon_{s})+2\alpha^{2}(3+4\upsilon_{s})+[(8\upsilon_{s}-1)-4\alpha^{2}(5+2\upsilon_{s})]g\\ +6(\alpha^{2}-1)(1+\upsilon_{s})g^{2}\\ 2\alpha^{2}+(1-4\alpha^{2})g+(\alpha^{2}-1)(1+\upsilon_{s})g^{2}\\ -3\left[\frac{8(\upsilon_{s}-1)+2\alpha^{2}(5-4\upsilon_{s})+[3(1-2\upsilon_{s})+6\alpha^{2}(\upsilon_{s}-1)]g}{-2\alpha^{2}+[(2-\upsilon_{s})+\alpha^{2}(1+\upsilon_{s})]g}\right] \end{cases},$$
(XI

Where $v_s = (3K_0 - 2G_0)/(6K_0 + 2G_0)$, and

$$g = \begin{cases} \frac{\alpha}{(1-\alpha^2)^{3/2}} \left(\arccos \alpha - \alpha \sqrt{1-\alpha^2} \right) (\alpha < 1) \\ \frac{\alpha}{(1-\alpha^2)^{3/2}} \left(\alpha \sqrt{1-\alpha^2} - \operatorname{arccosh} \alpha \right) (\alpha > 1) \end{cases}$$
(XII)

With the rock only including minerals and stiff pores as the background medium, the effective bulk and shear moduli are expressed as follows by considering the effect of soft micro-cracks:

$$K_{eff} = K_{stiff} / \left(1 + \frac{16(1 - (\upsilon_{stiff})^2 \Gamma)}{9(2 - \upsilon_{stiff})} \right)$$
 (XIII)

$$G_{eff} = G_{stiff} / \left(1 + \frac{32(1 - \upsilon_{stiff})(5 - \upsilon_{stiff})\Gamma}{45(2 - \upsilon_{stiff})} \right)$$
 (XIV)

Where $v_{\rm stiff} = (3K_{\rm stiff} G_{\rm stiff})/(6K_{\rm stiff} + 2G_{\rm stiff})$ is the Poisson's ratio of stiff pores. And Γ is the cumulative micro-crack density.

Given that the pressure-dependent effective moduli are closely related to the micro-crack density, the cumulative micro-crack density $\Gamma_p(\alpha)$ at each pressure can be fitted based on the measured elastic moduli and **Equations XIII** and **XIV** with the least-square regression method. Then, the quantitative relationship between micro-crack density and the effective pressure⁴⁶ is expressed as:

$$\Gamma_{p}(\alpha) = \Gamma^{i} e^{-p/\tilde{p}} \tag{XV}$$

Where Γ^i represents the initial micro-crack density at zero effective pressure; and \check{p} is a pressure constant with the same order of magnitude as the effective pressure p, which can be obtained by fitting data with **Equations XIII** and **XIV**.

We can obtain the distribution characteristics of microcrack porosity and density based on the lab-measured P- and S-wave velocities. The relationship between microcrack porosity ϕ_c and crack density Γ_p is described by David and Zimmerman⁴¹ as follows:

$$\varphi_c = \frac{4\pi\alpha_p}{3}\Gamma_p \tag{XVI}$$

In addition, the relationship between pore aspect ratio and the effective pressure is expressed as:

$$\alpha_p = \frac{4[1 - (\upsilon_{eff})^2]p}{\pi E_{eff}}$$
 (XVII)

Where $E_{\it eff}=3K_{\it eff}[1-2\upsilon_{\it eff}]$ is the effective Young's modulus under high confining pressure; and $\upsilon_{\it eff}=(3K_{\it eff}-2G_{\it eff})/(6K_{\it eff}+2G_{\it eff})$ is the effective Poisson's ratio under high confining pressure.

4.2. Inversion of micro-crack parameters

According to Equations VIII-IX, we first inverted the high-pressure velocities of three shale samples with different structures to estimate the aspect ratios of stiff pores. Since the measured velocities of the samples did not fully reach asymptotic values at 35 MPa, exponential curve fitting of the measured data was performed to estimate the high-pressure velocities. The confining pressure (P)-velocity fitting relationship of sample G1 is $V_p = 2628 \times P^{0.03116}$, $V_s = 1681 \times P^{0.01215}$. The confining pressure-velocity fitting relationship of sample G2 is $V_{\scriptscriptstyle p}$ = 2284* $P^{0.08616}$, $V_s = 1676*P^{0.0318}$. The confining pressurevelocity fitting relationship of sample G3 is $V_p = 4040 \text{*P}^{0.0341}$, $V_s = 2338*P^{0.0356}$. The porosity of the laminated sample G1 is 6.5%, that of the bedded sample G2 is 1.5%, and that of the massive sample G3 is 1.2%. The elastic moduli of grains (K0, G0) were obtained using the Voigt-Reuss-Hill theory for inverting high-pressure data, and the inversion parameters of high-pressure velocities are listed in Table 2. As expected, the inversion crack density/crack porosity is much higher for laminated shale than for bedded and massive shales, as shown in Table 2. The primary causes of crack development in laminated shale are as follows: Silt and clay laminae creates weak planes prone to forming bedding cracks, and oil expulsion during the thermal maturation of organic matter generates micro-cracks arranged parallel to bedding planes as shown in Table 1. Figure 6 shows the effective medium simulation results of P-wave and S-wave velocities for the laminated shale G1, bedded shale G2, and massive shale G3. The P-wave and S-wave velocities inverted based on the M-T theoretical model are in good agreement with the measured data within the error range. Notably, the model's predictions are more accurate for P-waves for than S-waves. These results validate the reliability of the model in predicting shale micro-crack parameters and demonstrate its effectiveness

Table 2. Inversion result for the high-pressure velocities

Sample ID	Туре	Porosity (%)	K0 (GPa)	G0 (GPa)	α	Crack density	Crack porosity
G1	Laminated shale	6.5	21.5	11	0.09	0.0051	6.38E-05
G2	Bedded shale	1.5	38	13	0.02	0.0042	4.49E-05
G3	Massive shale	1.2	39	21	0.16	0.0021	1.01E-05

in characterizing the elastic properties of shales with different structure types.

Figure 7 illustrates the porosity distribution of soft pores across aspect ratios for shales with distinct structures. The laminated shale (red) features the highest peak crack porosity, occurring at a relatively larger crack aspect ratio. The bedded shale (green) has a lower peak crack porosity than the laminated shale, while the massive shale (blue) shows the lowest peak crack porosity among the three. Across all aspect ratios shown, the laminated shale consistently maintains higher crack porosity than the bedded and massive shales. Figure 8 displays the cumulative crack density distribution of soft pores for the three shale types. The laminated shale has the largest cumulative crack porosity (6.38 \times 10⁻³%), followed by the bedded shale (4.49 \times 10⁻³%), and the massive shale (1.01 \times 10⁻³%) due to its slowest crack development and the lowest cumulative

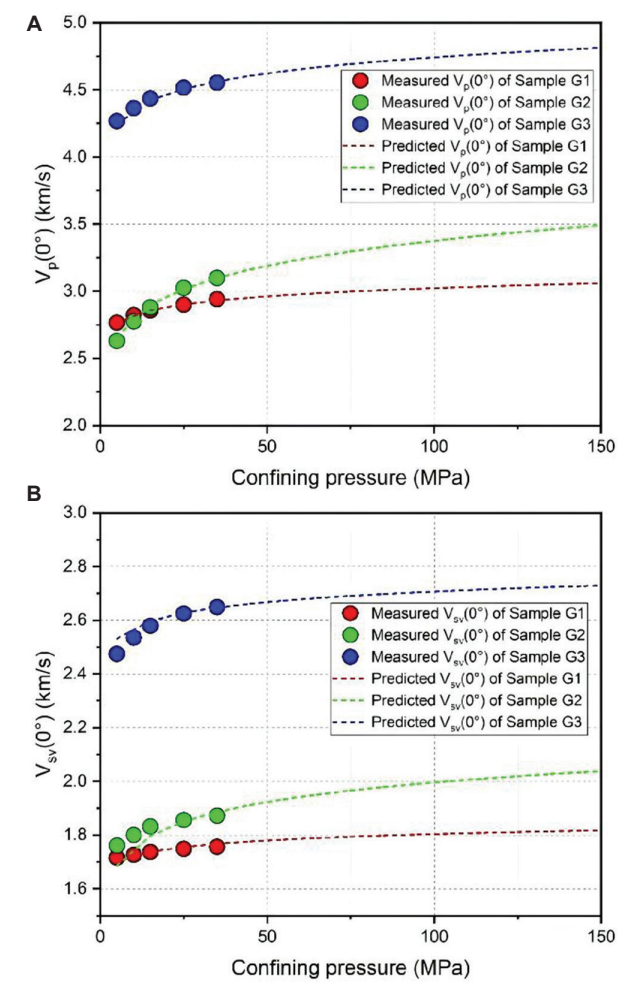


Figure 6. A comparison between the measured pressure-P-wave and S-wave velocities of the samples G1/G2/G3 and those inverted by the Mori-Tanaka model

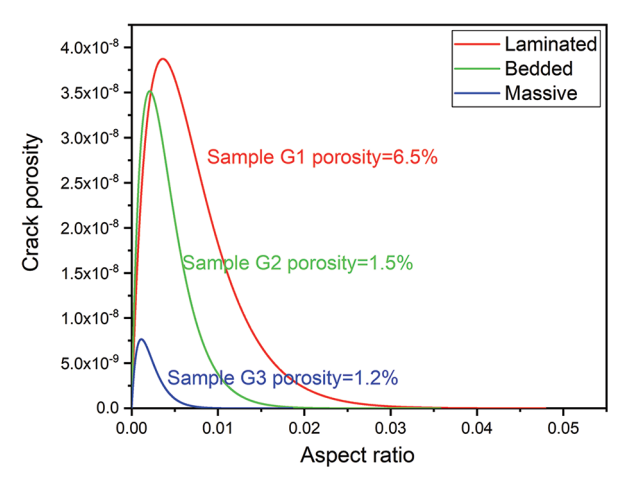


Figure 7. Crack porosity distribution as a function of aspect ratio for different structures

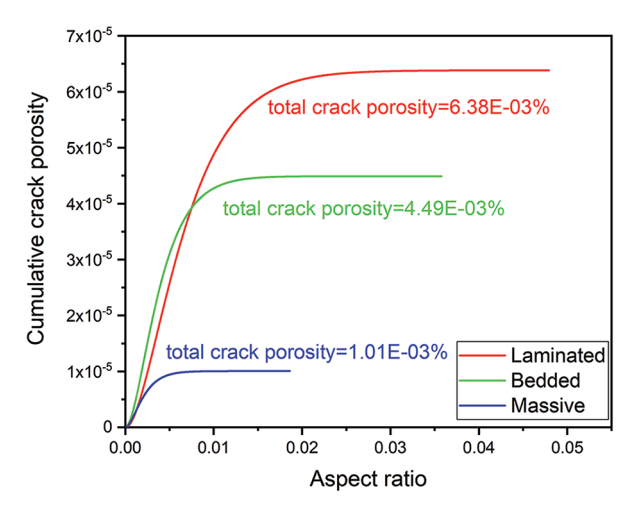


Figure 8. The relationship between cumulative crack porosity and crack aspect ratio for different structures

porosity. Overall, cumulative crack porosity rises initially and stabilizes, with the laminated shale having the highest values, the bedded shale intermediate, and the massive shale the lowest. As shown in Figure 4, the laminated shale exhibits a non-linear stress-sensitive curve (steep velocity-pressure response), while the bedded and massive shales show gentler stress-sensitive curve changes (gradual velocity-pressure response), reflecting their structural and mineralogical differences in pore compressibility.

Figure 9 illustrates the relationship between crack density and crack porosity for three different shale structures. Data points for the laminated shale are widely distributed, with crack porosity reaching approximately 0.015% and corresponding crack density around 0.012. This indicates extensive crack development in laminated shale. In contrast, data for the bedded shale cluster more

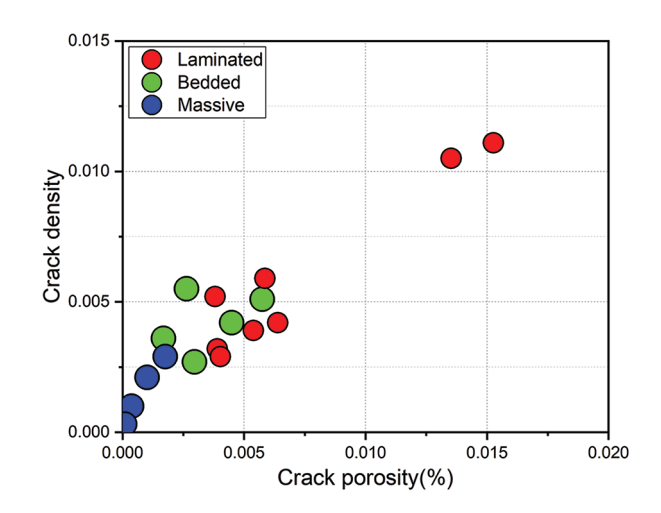


Figure 9. Crossplot of the relationship between crack density and crack porosity

tightly in the medium-to-low range, with crack porosity mostly below 0.006% and crack density typically below 0.006, suggesting moderate crack development. For the massive shale, data points concentrate near the origin, with crack porosity values mostly below 0.003% and crack density consistently below 0.003, indicating the poorest crack network development among the three types. As shown in Figure 1 and Table 1, the high clay mineral content in laminated shale (G1) results in strong clay orientation, forming bedding weak planes. In addition, during hydrocarbon generation and expulsion from organic matter maturation, pressure release along these weak planes generates numerous bedding-parallel cracks, leading to high crack porosity (reflecting interlaminar pores and cracks). Bedded shale (G2) exhibits distinct mud-sand interbedding but with slightly poorer bedding continuity and slightly higher mineral content (e.g., silty quartz) than G1. Bedding weak planes still dominate crack development (primarily bedding-parallel), but some cracks form due to stress concentration at mineral interfaces, resulting in lower crack and total porosity (1.5%) compared to laminated shale. Finally, massive shale (G3) lacks distinct bedding, is dominated by rigid minerals (quartz, feldspar), has low clay content, and exhibits dense intergranular cementation-all of which inhibit crack development, resulting in the lowest crack and total porosity. These results highlight the significant influence of shale structural differences on crack development characteristics, which cannot be overlooked.

4.3. Effects of micro-cracks on shale anisotropy

Analysis of the influencing factors of anisotropy in shale (Figures 10 and 11) reveals two distinct controlling patterns of shale anisotropy: One dominated by micro-crack

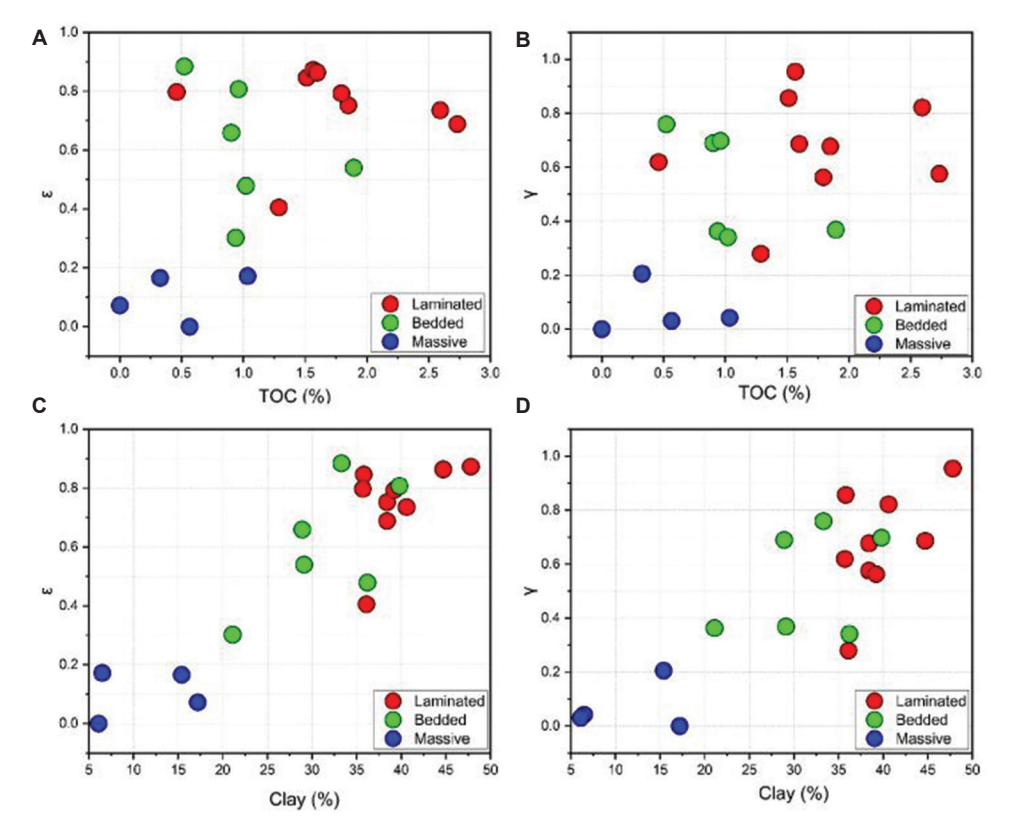


Figure 10. The influence of total organic carbon (TOC)/clay on anisotropic parameters. (A) The relationship between the anisotropy parameter ε and the TOC. (B) The relationship between the anisotropy parameter ε and the Clay. (D) The relationship between the anisotropy parameter γ and the clay.

development and the other by composition. As shown in Figure 10A and B, the Thomsen parameters ε and γ exhibit a clear positive correlation with TOC, particularly in laminated and bedded shales, indicating that organic matter content enhances intrinsic anisotropy. Similarly, Figures 10C and D demonstrate a strong dependence of ε and y on clay content, highlighting the essential role of clay mineral orientation in forming anisotropic backgrounds. Within this compositional framework, micro-crack porosity further differentiates the anisotropy degree among shale structures (Figure 11). Laminated shale, characterized by high clay content (average 40%) and moderate TOC, exhibits the strongest positive correlation between crack porosity (up to 0.015%) and Thomsen parameters ($\varepsilon = 0.3-0.8$; $\gamma = 0.2-1.0$). Results presented in Figure 1 and Table 1 suggest a synergistic effect between clay-induced intrinsic anisotropy and crack-related extrinsic anisotropy. The preferred orientation of clay minerals resulting from smectite-to-illite transformation establishes a foundation of intrinsic anisotropy, 47,48 while hydrocarbon-expulsion-induced micro-cracks, aligned parallel to bedding, further amplify the anisotropic expression.449 Bedded shale, with slightly lower clay

content (average 32%), comparable TOC, and lower crack porosity (<0.006%), shows moderate anisotropy (ϵ = 0.2–0.6; γ = 0.3–0.6). Its interlayered silty quartz disrupts clay fabric continuity, leading to less aligned micro-cracks and thus reduced anisotropy. In contrast, massive shale, with low clay content and minimal TOC, and the lowest crack porosity (<0.003%) exhibits near isotropy (ϵ , γ \rightarrow 0). The dominance of rigid minerals (quartz + feldspar >60%) and the absence of continuous bedding or organic alignment result in an isotropic elastic response, as predicted by Backus averaging theory for homogeneous media. Thus, shale anisotropy is co-controlled by composition (TOC and clay) and micro-structure (micro-crack development), with laminated shales exhibiting the most significant combined effect.

This study investigates the correlation between anisotropy and micro-cracks using the M-T theoretical model, providing valuable insights for exploration and development of lacustrine shale reservoirs. Specifically, in seismic data interpretation, integrating shale anisotropy characteristics and dynamic effects of micro-cracks can improve reservoir prediction accuracy. For example, the significant anisotropy and bedding-parallel

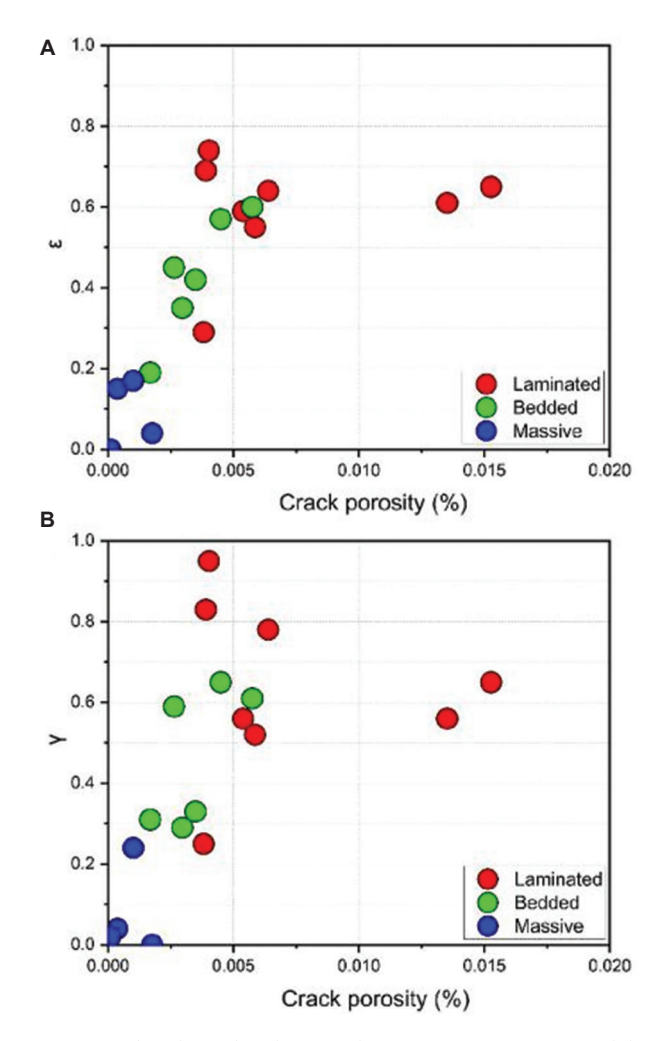


Figure 11. The relationships between the anisotropy parameter ε and the crack porosity (A), as well as between the anisotropy parameter γ and the crack porosity (B)

micro-cracks in laminated shale highlight the need for targeted exploration focus on such intervals. In addition, optimizing well locations to match dominant micro-cracks directions and considering anisotropy in fracturing designs can significantly enhance hydrocarbon recovery efficiency. Collectively, these findings provide critical, practice-oriented guidance for the efficient development of unconventional resources like shale oil and gas.

However, this study has some limitations. Firstly, due to limited core availability, only 4–6 samples were available for each structural type, potentially resulting in uncertainty when extrapolating to the entire reservoir. Future work should increase the sample size and combine digital rock physics to reduce statistical bias. Then, the model assumes an ideal uniform distribution of microcracks in the medium, which fundamentally differs from

the complex heterogeneous fracture networks observed in real shales. This may lead to prediction biases in anisotropy characteristics. Therefore, future research could refine the model by incorporating both uniformly distributed random fractures and preferentially oriented bedding-parallel cracks, thereby capturing the heterogeneous characteristics of real reservoirs more accurately.

5. Conclusion

In this study, 17 shale samples from a Cretaceous lacustrine reservoir were classified into three structural types: Laminated, bedded, and massive, based on their micro-fabric characteristics. Ultrasonic velocity measurements were performed on 17 pairs of shale plugs under varied confining pressures to quantitatively analyze the relationship between micro-crack parameters and elastic anisotropy. The results indicate that the stress sensitivity of bedding-normal velocities relies on rock sedimentary structure, in the order of: laminated > bedded > massive. Specifically, laminated shales exhibit the most pronounced anisotropic properties, followed by bedded shales, while massive shales display the weakest anisotropic characteristics. Measured velocities showed good agreement with predictions from the M-T model, validating its applicability for structurally diverse shales. Furthermore, a trend was observed where a higher crack aspect ratio correlates with higher crack porosity in nonclosable pores, a feature predominantly found in laminated samples. As crack density and porosity increase, the degree of anisotropy in lacustrine shales intensifies. Among the three structural types, laminated shales exhibit the highest crack porosity, which is consistent with their pronounced anisotropic characteristics. Within the studied lacustrine shales, sedimentary structure appears to be the dominant controlling micro-crack development anisotropy, although clay and TOC also play contributory roles. This study has specific guiding significance for seismic anisotropy inversion, hydraulic fracturing design, or well logging interpretation.

Acknowledgments

We gratefully acknowledge the guidance of Professor Dehua Han from the Rock Physics Laboratory at the University of Houston, USA, in this project.

Funding

This research was supported by the National Natural Science Foundation of China (grant number: 42430810).

Conflict of interest

The authors declare that they have no conflicts of interest.

Author contributions

Conceptualization: Wenhui Tan, Yang Wang Data curation: Wenhui Tan, Yang Wang

Formal analysis: Weihua Liu Investigation: Weihua Liu Methodology: Wenhui Tan Supervision: Hui Shen Visualization: Weihua Liu

Writing-original draft: Wenhui Tan Writing-review & editing: Yang Wang

Availability of data

The data supporting this study are available from the corresponding author on reasonable request.

References

 Zou CN, Yang Z, Zhu RK, et al. Progress in China's unconventional oil & gas exploration and development and theoretical technologies. Acta Geol Sin. 2015;89(6):979-1007.

doi: 10.1111/1755-6724.12491

 Jin ZJ, Wang GP, Liu GX, et al. Research progress and key scientific issues of continental shale oil in China. Acta Petrol Sin. 2021;42(7):821-835.

doi: 10.7623/syxb202107001

3. Li MW, Ma XX, Jin ZJ, et al. Diversity in the lithofacies assemblages of marine and lacustrine shale strata and significance for unconventional petroleum exploration in China. Oil Gas Geol. 2022;43(1):1-25.

doi: 10.11743/ogg20220101

 Vernik L, Nur A. Ultrasonic velocity and anisotropy of hydrocarbon source rocks. *Geophysics*. 1992;57:727-735.

doi: 10.1190/1.1443286

- 5. Vernik L, Landis C. Elastic anisotropy of source rocks: Implications for hydrocarbon generation and primary migration. *AAPG Bull.* 80(4):531-544.
- 6. Wright J. The effects of transverse isotropy on reflection amplitudes versus offset. *Geophysics*. 1987;52:564-567.

doi: 10.1190/1.1442325

7. Sayers CM. Seismic anisotropy of shales. *Geophys Prospect*. 2005;53:667-676.

doi: 10.4236/ijg.2016.73027

8. Vernik L. Chapter 3: Seismic Rock properties and rock physics. In: Vernik L, editor. *Seismic petrophysics in Quantitative Interpretation*. Houston: Society of Exploration Geophysicists; 2016. p. 43-86.

doi: 10.1190/1.9781560803256.ch3

9. Zoback MD, Kohli AH. Unconventional Reservoir Geomechanics: Shale Gas, Tight Oil, and Induced Seismicity.

Cambridge: Cambridge University Press; 2019.

 Yin XY, Zong ZY, Wu GC. Research on seismic fluid identification driven by rock physics. Sci Chin Earth Sci. 2015;58:159-171.

doi: 10.1007/s11430-014-4992-3

 Chen HZ, Yin XY, Gao JH, Liu BY, Zhang GZ. Seismic inversion for underground fractures detection based on effective anisotropy and fluid substitution. Sci China Earth Sci. 2015;58:805-814.

doi: 10.1007/s11430-014-5022-1

 Liu Z, Zhang F, Li X. Elastic anisotropy and its influencing factors in organic-rich marine shale of southern China. Sci China Earth Sci. 2019;62:1805-1818.

doi: 10.1007/s11430-019-9449-7

13. Vernik L, Liu X. Velocity anisotropy in shales: A petrophysical study. *Geophysics*. 1997;62(2):521-532.

doi: 10.1190/1.1444162

 Sone H, Zoback MD. Mechanical properties of shale-gas reservoir rocks-Part 1: Static and dynamic elastic properties and anisotropy. *Geophysics*. 2013;78:D381-D392.

doi: 10.1190/geo2013-0050.1

15. Hornby BE, Schwartz LM, Hudson JA. Anisotropic effective medium modeling of the elastic properties of shales. *Geophysics*. 1994;59:1570-1583.

doi: 10.1190/1.1443546

16. Sayers CM. The elastic anisotrophy of shales. *J Geophys Res*. 1994;99:767-774.

doi: 10.1029/93JB02579

 Lonardelli I, Wenk HR, Re Y. Preferred orientation and elastic anisotropy in shales. *Geophysics*. 2007;72:D33-D40.

doi: 10.1190/1.2435966

18. Wenk HR, Lonardelli I, Franz H, Nihei K, Nakagawa S. Preferred orientation and elastic anisotropy of illite-rich shale. *Geophysics*. 2006;72:E69-E75.

doi: 10.1190/1.2432263

- Bandyopadhyay K. Seismic Anisotropy-Geological Causes and its Implications to Reservoir Geophysics. Dissertation for Doctoral Degree. Palo Alto: Stanford University; 2009.
- Qian K, Zhang F, Chen S, Li X, Zhang H. A rock physics model for analysis of anisotropic parameters in a shale reservoir in Southwest China. *J Geophys Eng.* 2016;13:19-34.

doi: 10.1088/1742-2132/13/1/19

21. Zhang F, Li X, Qian K. Estimation of anisotropy parameters for shale based on an improved rock physics model, part 1: Theory. *J Geophys Eng.* 2017;14:143-158.

doi: 10.1088/1742-2140/14/1/143

22. Zhang F. Estimation of anisotropy parameters for shales based on an improved rock physics model, part 2: Case study. *J Geophys Eng.* 2017;14:238-254.

doi: 10.1088/1742-2140/aa5afa

23. Zhang F. A modified rock physics model of overmature organicrich shale: Application to anisotropy parameter prediction from well logs. *J Geophys Eng.* 2019;16:92-104.

doi: 10.1093/jge/gxy008

24. Tan KJ, Deng JX, Liu ZH, Sun X. Rock physical properties and variation patterns of Chang 7 lacustrine shale oil reservoir in the Triassic Yangchang Formation, Ordos Basin. *Chinese J Geophys.* 2025;68(2):652-667.

doi: 10.6038/cjg2023Q0862

25. Liu WH, Wang Y, Shen H, Li M, Fan WH. Ultrasonic velocity anisotropy of Jurassic shales with different lithofacies. *J Geophys Eng.* 2024;21(4):1103-1118.

doi: 10.1093/jge/gxae061

 Vernik L. Microcrack-induced versus intrinsic elastic anisotropy in mature HC-source shales. *Geophysics*. 1993;58(11):1703-1706.

doi: 10.1190/1.1443385

27. Ciz R, Shapiro SA. Stress-dependent anisotropy in transversely isotropic rocks: Comparison between theory and laboratory experiment on shale. *Geophysics*. 2009;74(1):D7-D12.

doi: 10.1190/1.3008546

28. Sarout J, Molez L, Gueguen Y, Hoteit N. Shale dynamic properties and anisotropy under triaxial loading: Experimental and theoretical investigations. *Phys Chem Earth Parts A/B/C*. 2007;32(8):896-906.

doi: 10.1016/J.PCE.2006.01.007

29. Sayers C, Munster J, King MS. Stress-induced ultrasonic anisotrophy in Berea sandstone. *Int J Rock Mech Mining Sci Geomech Abstr.* 1990,27:429-436.

doi: 10.1016/0148-9062(90)92715-Q

30. Kohli AH, Zoback MD. Frictional properties of shale reservoir rocks. *J Geophys Res Solid Earth*. 2013;118(9):5109-5125.

doi: 10.1002/jgrb.50346

31. Yan BH, Zhao JG, Xiao ZJ, *et al.* Analysis of elastic properties and anisotropic rock physics modeling of Qianjiang Formation shale. *Chinese J Geophys.* 2024;67(7):2802-2819.

doi: 10.6038/cjg2022Q0724

- 32. Zhang JC, Lin LM, Li YX, Tang X, Zhu LL, Xin YW. Classification and evaluation of shale oil. *Earth Sci Front*. 2012;19(5):322-331.
- 33. Liu B, Lyu Y, Ran Q, et al. Geological conditions and exploration potential of shale oil in Qingshankou

Formation, Northern Songliao Basin. Oil Gas Geol. 2014;35(2):280-285.

doi: 10.11743/ogg20140216

34. Liu B, Shi JX, Fu XF, *et al.* Petrological characteristics and shale oil enrichment of lacustrine fine-grained sedimentary system: A case study of organic-rich shale in first member of Cretaceous Qingshankou Formation in Gulong Sag, Songliao Basin, NE China. *Petrol Explor Dev.* 2018;45(5):828-838.

doi: 10.1016/S1876-3804(18)30091-0

35. Lazar OR, Bohacs KM, Macquaker JH, Schieber J, Demko T. Capturing key attributes of fine-grained sedimentary rocks in outcrops, cores, and thin sections: Nomenclature and description guidelines. *J Sediment Res.* 2015;85(3):230-246.

doi: 10.2110/jsr.2015.11

36. Vernik L. Hydrocarbon generation-induced microcracking of source rocks. *Geophysics*. 1994;59(4):555-563.

doi: 10.1190/1.1443616

 Sun LD, Wang XJ, Feng ZH, et al. Formation mechanisms of nano-scale pores/fissures and shale oil enrichment characteristics for Gulong shale, Songliao Basin. Oil Gas Geol. 2023;44(6):1350-1365.

doi: 10. 11743/ogg20230602

- He WY, Zhao Y, Zhong JH, Sun NL. Characteristics and significance of micron pores and micron fractures in shale oil reservoirs of Cretaceous Qingshankou Formation in Gulong sag, Songliao Basin. *Lithol Reserv.* 2024;36(3):1-18.
- 39. Wang Z. Seismic anisotropy in sedimentary rocks, part 1: A single plug laboratory method. *Geophysics*. 2002;67(5):1415-1422.

doi: 10.1190/1.1512787

40. Thomsen L. Weak elastic anisotropy. *Geophysics*. 1986;51(10):1954-1966.

doi: 10.1190/1.1442051

 David EC, Zimmerman RW. Pore structure model for elastic wave velocities in fluid-saturated sandstones. *J Geophys Res*. 2012;117(B7): B07210.

doi: 10.1029/2012JB009195

42. Lo TW, Coyner KB, Toksöz MN. Experimental determination of elastic anisotropy of Berea sandstone, Chicopee shale, and Chelmsford granite. *Geophysics*. 1986;51(1):164-171.

doi: 10.1190/1.1442029

- 43. Johnston JE, Christensen NI. Seismic anisotropy of shales. *J Geophys Res.* 1995;100:5991-6003.
- Mori T, Tanaka K. Average stress in matrix and average elastic energy of materials with misfitting inclusions. *Acta Metall.* 1974;21(5):571-574.

- doi: 10.1016/0001-6160(73)90064-3
- 45. Zhang L, Ba J, Fu LY, Carcione José M, Cao CH. Estimation of pore microstructure by using the static and dynamic moduli. *Int J Rock Mech Min Sci.* 2019;113:24-30.
 - doi: 10.1016/j.ijrmms.2018.11.005
- 46. Shapiro SA. Elastic piezosensitivity of porous and fractured rocks. *Geophysics*. 2003;68(2):482-486.
 - doi: 10.1190/1.1567215
- 47. Kaarsberg EA. Introductory studies of natural and artificial argillaceous aggregates by sound-propagation and x-ray diffraction methods. *J Geol.* 1959;67(4):447-472.
 - doi: 10.1086/626597
- 48. Wenk HR, Voltolini M, Mazurek M, Loon LRV, Vinsot A.

- Preferred orientations and anisotropy in shales: Callovo-oxfordian shale (France) and Opalinus clay (Switzerland). *Clays Clay Miner*. 2008;56(3):285-306.
- doi: 10.1346/CCMN.2008.0560301
- 49. Curtis JB. Fractured shale-gas systems. AAPG Bull. 2002;86:1921-1938.
- Backus GE. Long-wave elastic anisotropy produced by horizontal layering. *J Geophys Res.* 1962;67(11):4427-4440.
 doi: 10.JZ067i011p04427
- 51. Mavko G, Mukerji T, Dvorkin J. *The Rock Physics Handbook: Tools for Seismic Analysis of Porous Media*. 2nd ed. Cambridge: Cambridge University Press; 2009.
 - doi: 10.1017/CBO9780511626753